Journal of Applied Fluid Mechanics , Vol. 9, No. 4, pp. 2009-2023, 2016.
Available online at www.jafmonline.net, ISSN 1735-3572, EISSN 1735-3645.
DOI: 10.18869/acadpub.jafm.68.235.24117

Numerical Simulation of the Turbulent Flow around an Oval-Sail

O. Guerri[1,2†], E. Liberge[2] and A. Hamdouni[2]

[1] *Centre de Developpement des Energies Renouvelables, BP 62, Route de l'Observatoire, Bouzareah, CP 16340, Alger, Algeria*

[2] *LaSIE, Universite de La Rochelle, Avenue Michel Crepeau, 17042 La Rochelle Cedex 1, France*

† *Corresponding Author Email*: *o.guerri@cder.dz*

(Received October, 6, 2014; accepted September, 15, 2015)

ABSTRACT

This paper presents numerical study of an oval-sail, a bluff-body equipped with a grid all along the span. Suction based flow control is applied to this body that is developed for wind assisted ship propulsion. First, a choice of numerical turbulence model is discussed through results of an oval-sail without suction. Three turbulence models are applied: the R_{ij} SSG, the R_{ij} EBRSM and the $v2f$ model. Then, computations are performed for the oval-sail fitted with suction grid. These last simulations are carried out with the low-Reynolds-number R_{ij} EBRSM turbulence model. The influence of the grid geometry on the oval-sail aerodynamic performances is highlighted. All simulations are carried out for the sail set at zero incidence. The Reynolds number based on the free stream velocity and the profile chord is $Re = 510^5$. Results are compared to available experimental data.

Keywords: Flow control; Oval-sail; Turbulence; Numerical study; URANS; Suction.

NOMENCLATURE

c	chord	N_z	cell number in the spanwise direction
C_D	drag coefficient	p	pressure at the sail surface
C_{DS}	drag coefficient of the sail with suction	p_∞	pressure in the free stream
C_L	lift coefficient	Re	Reynolds number
C_{LS}	lift coefficient of the sail with suction	r_{11}	streamwise Reynolds stress component
C_P	pressure coefficient	r_{12}	shear stress component
C_Q	suction coefficient	r_{22}	transverse Reynolds stress component
$C_{\mu cyl}$	momentum coefficient	St	Strouhal number
D	cylinder diameter	t	time
f	vortex shedding frequency	t^*	adimensional time
F_x	X component of the fluid force	u	velocity
F_y	Y component of the fluid force	U_{asp}	suction velocity
Go	Gortler number	U_∞	free stream velocity
I	turbulence intensity		
k_∞	free stream turbulence	Δt	time step
L	span of the sail	Δt^*	adimensional time step
L_{ref}	reference lenght	θ	angle width of the suction grid
l_s	slot width	θ_{cyl}	suction location on the cylinder surface
n	slot number	μ	laminar dynamic viscosity coefficient
N	cell number	μ_t	turbulent dynamic viscosity coefficient
N_{cyl}	cell number at the cylinder surface	ρ	fluid density

1. INTRODUCTION

In recent years, there has been a renewed interest in wind assisted ship propulsion. Therefore, flow control systems are applied to improve the aerodynamic performances of the profiles used for that purpose. Depending on the target application, there are different techniques to control the boundary layer, passive or active (Muddada and Patnaik 2010), based on blowing or suction (Favier and Kourta 2006), (Huang *et al.* 2004), (Viswanath *et al.* 2000) or on synthetic jets (M. Amitay and A. Glezer 2002). Flow control of the wake behind circular cylinder has been extensively investigated to reduce vortex shedding and thereby flow-induced vibrations. For that purpose, Bao and Tao (2013) used passive dual plates attached at the rear surface of a cylinder, Lim and Lee (2004) installed O-rings as surface protrusions along the span of a circular cylinder or more recently, Reddy *et al.* (2013) applied two small counter-rotating control cylinders in the vicinity of a main circular cylinder. In aeronautics, the issues are to delete or delay the separation of the boundary layer in order to enhance the aerodynamic profile performances (by reducing the drag and improving lift force) and to reduce noise (Favier and Kourta 2006). When the control is applied in the automotive industry, similar intended effects are expected (Boccaletti *et al.* 2009). In wind turbines, aerodynamic control is mainly used to keep rotational speed and power output of the turbines within a certain range. Then usually, active control based on blade pitch variation or passive control based on dynamic stall are used. In Bai *et al.* (2011), two types of flow control for wind turbine airfoils, blade airfoil with flow deflector and blade tip with vortex diffusers, were proposed to increase lift, reduce drag, lower noise, avoid separation at a high angle of attack and delay stall.

In devices developed for ship propulsion, the intended effect is to reduce drag and improve the lift force. Among the developed devices used in wind assisted ship propulsion, some of them were based on Magnus effect as for the rotor-driven catamaran developed at the University of Flensburg (Germany) or the cargo ship of ENERCON (Ireland). A review of Magnus effect research and development in aeronautics can be found in Jost Seifert (2012). Other wind assisted ship propulsion devices were based on suction control as in the Alcyone turbo-sail of Malavard (1984). The latter showed that the turbo-sail lift coefficient could attain values larger than 8.0 at high incidence. These results were obtained by calculations based on potential flow theory and wind tunnel experiment. The influence of the angle of attack and that of the suction flow rate were studied. However, except the work presented by this author, to the authors knowledge, there are no extensive study (numerical or experimental) applied on such body. Moreover, in Malavard (1984), the shape of the turbo-sail and the geometry of the grid intake are not precisely defined. Furthermore this turbo-sail is equipped with a spoiler which causes complex flows in the wake. Therefore, accurate predictions of the fluid flow are needed if one intend to utilize such device. This is the aim of the present study where numerical simulations of the flow around an an oval-sail are carried out. The oval-sail section is similar to the Alcyone turbo-sail, with a thickness of 66 %. This bluff body is equipped with a flap at the trailing edge and with an intake grid on the upper surface, all along the span. The oval-sail is hollow, the interior being cylindrical (Fig. 1). Boundary layer suction control is applied, air suction being carried out continuously at the circular base.

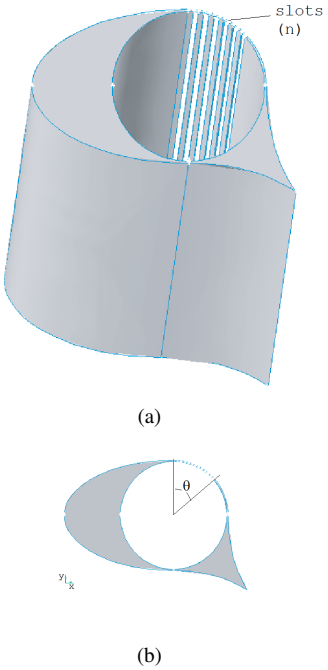

Fig. 1. Scheme of the oval-sail.

The work presented here focuses on the flow control and the grid intake geometry on the aerodynamic performances of the oval-sail. It is noteworthy that this is not a closed-loop control investigation. This study is conducted in an open-loop manner where the parameters remain fixed regardless of changes in the state of the flow.

The paper is organized as follows: The numer-

ical approach with details of turbulence models are depicted in section 2.. In section 3., the results obtained for a circular cylindre are presented as a model validation test. Then in section 4., lift and drag coefficients, the mean flow topology and vortex shedding frequency obtained for the oval sail without suction with three turbulence models are compared. The influence of the grid intake geometry on the aerodynamic perfomance of the oval-sail is discussed in section 5.. Calculated lift and drag coefficients are compared to available data.

2. NUMERICAL APPROACH

The numerical simulations of the flow around the body are based on the solution of the unsteady Reynolds averaged Navier-Stokes equations. As limited data are available in the literature, three turbulence models are compared: the $k-\varepsilon/\overline{v'^2}f$ (or $v2f$) model as developed by Laurence *et al.* (2004), the Reynolds Stress Model of Speziale *et al.* (1991) or R_{ij} SSG model and the Elliptic-Blending Reynolds Stress Model or R_{ij} EBRSM of Manceau and Hanjalic (2002). These models are selected for the following reasons: According to Basara *et al.* (1997), the R_{ij} SSG model improves significantly the predictions of steady and unsteady flows compared to the $k-\varepsilon$ model and the flow field is reasonably well calculated. Thus it provides reasonable results for a wide range of applications as recirculating flows or vortex shedding calculations, so it would be suitable for the flow computations around the oval sail. However, the R_{ij} SSG model is a high-Reynolds-numbers turbulence model. Therefore for better resolution of near wall effects, the R_{ij} EBRSM, a low-Reynolds-number model based on Reynolds stress transport equations, is also used. The $v2f$ model is a low-Reynolds numbers eddy viscosity turbulence model where near wall treatments are similar to the R_{ij} EBRSM model. When using the $v2f$ model one solves less equations than with R_{ij} models but the former as the EBRSM are recent models. The R_{ij} SSG model is than used as reference model. The three turbulence model equations as implemented in the CFD code (*code_saturne version 2.3*) are describe in the next section.

2.1 Turbulence Models

The $v2f$ model It is a low-Reynolds-number turbulence model that uses an elliptic relaxation approach which accounts for the wall blocking effects on the Reynolds stresses. This model is based on three transport equations for k, the turbulent kinetic energy, ε, the turbulent dissipation, $\overline{v'^2}$, the normal component of the Reynolds stress tensor and on an elliptic equation for f, the source term of $\overline{v'^2}$. Far from the wall, it is assumed that the turbulence is isotropic and the standard $k-\varepsilon$ equations are then applied. Different versions of the $v2f$ model have been developed since it was introduced by Durbin. The model used in this work was proposed by Laurence *et al.* (2004). It is based on a change of variables from $\overline{v'^2}$ to $\varphi = \overline{v'^2}/k$ that lead to a boundary value problem with homogeneous boundary conditions, fixed-sign source terms and a modified equation for f being $\overline{f}$ to improve the model robustness. The equations of this model write as:

$$\frac{\partial k}{\partial t} + u_i \frac{\partial k}{\partial x_j} = P - \varepsilon + \frac{\partial}{\partial x_i}\left[\left(\nu + \frac{\nu_t}{\sigma_k}\right)\frac{\partial k}{\partial x_i}\right] \quad (1)$$

$$\frac{\partial \varepsilon}{\partial t} + u_i \frac{\partial \varepsilon}{\partial x_j} = \frac{1}{\tau}\left(C_{\varepsilon 1} P - C_{\varepsilon 2}\varepsilon\right) + \frac{\partial}{\partial x_i}\left[\left(\nu + \frac{\nu_t}{\sigma_k}\right)\frac{\partial \varepsilon}{\partial x_i}\right] \quad (2)$$

$$\frac{\partial \varphi}{\partial t} + u_i \frac{\partial \varphi}{\partial x_j} = \overline{f} - P\frac{\varphi}{k} + \frac{2}{k}\frac{\nu_t}{\sigma_k}\frac{\partial \varphi}{\partial x_i}\frac{\partial k}{\partial x_j} + \frac{\partial}{\partial x_i}\left[\frac{\nu_t}{\sigma_k}\frac{\partial \varphi}{\partial x_i}\right] \quad (3)$$

$$L^2 \frac{\partial^2 \overline{f}}{\partial x_i^2} - \overline{f} = \frac{1}{\tau}(C_1 - 1)\left[\varphi - \frac{2}{3}\right] - C_2\frac{P}{k} - \frac{2}{\tau}\frac{\nu}{\varepsilon}\frac{\partial \varphi}{\partial x_i}\frac{\partial k}{\partial x_j} - \nu\frac{\partial^2 \varphi}{\partial x_i^2} \quad (4)$$

where $P = 1/2\,P_{kk}$ represents the turbulent energy production. L and τ are the turbulent lenght and time scale respectively defined as:

$$L = C_L \max\left[\frac{k^{3/2}}{\varepsilon}, C_\eta \frac{\nu^{3/4}}{\varepsilon^{1/4}}\right] \quad (5)$$

$$\tau = \max\left[\frac{k}{\varepsilon}, C_\tau\sqrt{\frac{\nu}{\varepsilon}}\right] \quad (6)$$

The model constants are summarized in Table 1 and the term $C_{\varepsilon 1}$ is given by the following relation:

$$C_{\varepsilon 1} = C_{\varepsilon 1}^0\left[1 + a_1\sqrt{\frac{1}{\varphi}}\right] \quad (7)$$

Table 1 Constants used for the $v2f$ model

a_1	C_1	C_2	C_L	C_τ
0.05	1.4	0.3	0.25	6
C_η	$C^0_{\varepsilon 1}$	$C_{\varepsilon 2}$	C_μ	σ_k
110.	1.4	1.85	0.22	1.00

The R_{ij} SSG model This model is quadratically non linear in the anisotropy tensor (Speziale *et al.* 1991). It uses a Reynolds stress approach that improve the pressure-rate-of strain in the Reynolds stress equations by taking into account the non-linear return to isotropy. The transport equation for r_{ij} writes as:

$$\frac{\partial r_{ij}}{\partial t} + u_k \frac{\partial r_{ij}}{\partial x_k} = D^{\nu}_{ij} + D^{T}_{ij} + \phi_{ij} + P_{ij} + \varepsilon_{ij} \quad (8)$$

where D^{ν}_{ij} and D^{T}_{ij} are the viscous and turbulent diffusion term respectively, P_{ij} the production term, ε_{ij} the dissipation term and ϕ_{ij} is the pressure redistribution term:

$$\begin{aligned}\phi_{ij} = &-\left(C_1\varepsilon + C_1^* P\right) b_{ij} \\ &+ C_2\varepsilon\left(b_{ik}b_{ij} - \frac{1}{3}b_{ij}b_{ij}\delta_{ij}\right) \\ &+ \left(C_3 - C_3^*\sqrt{b_{kl}b_{kl}}\right) kS_{ij} \\ &+ C_4 k\left(b_{ik}S_{jk} + b_{jk}S_{ik} - \frac{2}{3}b_{kl}S_{kl}\delta_{ij}\right) \\ &+ C_5 k\left(b_{ik}\Omega_{jk} + b_{jk}\Omega_{ik}\right) \end{aligned} \quad (9)$$

where b_{ij} is the anisotropic Reynolds tensor

$$b_{ij} = \frac{r_{ij}}{k} - \frac{2}{3}\delta_{ij}$$

S_{ij} and Ω_{ij} are mean stress and rotational tensor, respectively:

$$S_{ij} = \frac{1}{2}\left(\frac{\partial u_i}{\partial x_j} + \frac{\partial u_j}{\partial x_i}\right) \qquad \Omega_{ij} = \frac{1}{2}\left(\frac{\partial u_i}{\partial x_j} - \frac{\partial u_j}{\partial x_i}\right)$$

The production and dissipation terms of the r_{ij} equation write as:

$$P_{ij} = -2r_{ij}\frac{\partial u_i}{\partial x_j} \qquad \varepsilon_{ij} = -\frac{2}{3}\varepsilon\delta_{ij}$$

The ε equation of this model is:

$$\begin{aligned}\frac{\partial \varepsilon}{\partial t} + u_i\frac{\partial \varepsilon}{\partial x_j} = &\frac{1}{\tau}\left(C_{\varepsilon 1}P - C_{\varepsilon 2}\frac{\varepsilon^2}{k}\right) \\ &+ \frac{\partial}{\partial x_i}\left(C_\varepsilon \frac{k}{\varepsilon} r_{ij}\frac{\partial u_i}{\partial x_i}\right)\end{aligned} \quad (10)$$

$C_{\varepsilon 1}$ is given by the relation:

$$C_{\varepsilon 1} = C^0_{\varepsilon 1}\left[1 + a_1\frac{\varepsilon}{k}\right] \quad (11)$$

The constants of this model are summarized in Table 2.

Table 2 Constants used for the R_{ij} SSG model

C_1	C_1^*	C_2	C_3	C_3^*
1.7	-1.05	0.9	0.8	0.65
C_4	C_5	C_ε	$C^0_{\varepsilon_1}$	$C_{\varepsilon 2}$
0.625	0.20	0.18	1.44	1.83

The EBRSM model This model adds a blending parameter between the near wall region and the homogeneous one to the pressure and dissipation terms. In the transport equation for r_{ij}, the pressure redistribution term, ϕ_{ij}, and the dissipation term, ε_{ij}, are modified as follow:

$$\phi_{ij} = (1-\alpha^3)\phi^w_{ij} + \alpha^3\phi^h_{ij} \quad (12)$$

$$\varepsilon_{ij} = (1-\alpha^3)\varepsilon^w_{ij} + \alpha^3\varepsilon^h_{ij} \quad (13)$$

where the indices w and h designate the near wall and homogeneous term respectively. The blending parameter α is obtained from the solution of an elliptic equation:

$$\alpha - L^2\nabla^2\alpha = 1 \quad (14)$$

The near wall terms are described by the following equations:

$$\varepsilon^w_{ij} = \frac{r_{ij}}{k}\varepsilon \quad (15)$$

$$\begin{aligned}\phi^w_{ij} = &\\ &-5\frac{\varepsilon}{k}\left(r_{ik}n_jn_k + r_{jk}n_in_k - \frac{1}{2}r_{kl}n_kn_l\left(n_in_j - \delta_{ij}\right)\right)\end{aligned} \quad (16)$$

where n is the unit wall-normal vector:

$$n = \frac{\nabla\alpha}{\|\nabla\alpha\|} \quad (17)$$

The expressions of ε^h_{ij} and φ^h_{ij} are based on the R_{ij} SSG model:

$$\varepsilon^h_{ij} = \frac{2}{3}\varepsilon\delta_{ij} \quad (18)$$

$$\phi_{ij}^{h} = -\left(C_1\varepsilon + C_1^*P\right)b_{ij} + \left(C_3 - C_3^*\left(b_{mn}b_{mn}\right)^{1/2}\right)kS_{ij} + C_4k\left(b_{ik}S_{jk} + b_{jk}S_{ik} - \frac{2}{3}b_{mn}S_{mn}\delta_{ij}\right) + C_5k\left(b_{ik}\Omega_{jk} + b_{jk}\Omega_{ik}\right) \quad (19)$$

The ε equation of this model is:

$$\frac{\partial\varepsilon}{\partial t} + u_i\frac{\partial\varepsilon}{\partial x_j} = \frac{1}{\tau}\left(C_{\varepsilon1}P - C_{\varepsilon2}\varepsilon\right) + \frac{\partial}{\partial x_i}\left[\tau\frac{C_\mu}{\sigma_\varepsilon}r_{ij}\frac{\partial\varepsilon}{\partial x_i}\right] \quad (20)$$

where $C_{\varepsilon1}$ is defined by the following equation:

$$C_{\varepsilon1} = C_{\varepsilon1}^0\left[1 + a_1\left(1-\alpha^3\right)\frac{P}{\varepsilon}\right] \quad (21)$$

The other terms have the same definition as above however the model constants are different (see Table. 3).

Table 3 Constants used for the R_{ij} EBRSM

C_1	C_1^*	C_2	C_3	C_3^*	C_4
1.7	0.9	0.	0.80	0.65	0.625
C_5	a_1	C_L	C_τ	C_η	
0.20	0.10	0.122	6.0	80	

2.2 Solved Equations

It is assumed that local velocities and Mach numbers are low so that compressibility effects are neglected. The generic formulation of the transport equation writes as:

$$\frac{\partial\rho\psi}{\partial t} + div\left((\rho\vec{v})\psi\right) = div\left(\Gamma\vec{grad}\psi\right) + P_\psi + D_\psi + S \quad (22)$$

where: $\psi = \{1, u, v, w, k, \varepsilon, \varphi \text{ or } r_{ij}\}$. When ψ is one of the time averaged velocity components, $P_\psi = -\vec{grad}\,p$, $D_\psi = 0$ and $S = 0$. For turbulence equations ($\psi = k, \varepsilon, \varphi$ or r_{ij}), P_ψ is the production term, D_ψ is the destruction term and S is the source term.

2.3 Boundary Conditions

Inlet conditions are specified at West boundary of the computational domain having defined the free stream velocity, U_∞ and turbulence quantities, the free stream turbulence energy, k_∞ and the dissipation rate of turbulence, ε_∞. The latter are defined as $k_\infty = 1.5U_\infty^2I^2$ and $\varepsilon_\infty = 10C_\mu k_\infty^{3/2}/(\kappa L_{ref})$ where I is the turbulence intensity, L_{ref} is the reference chord length ($L_{ref} = c$), C_μ and κ are constants ($C_\mu = 0.9$ and $\kappa = 0.42$). Outflow condition is defined at East boundary by setting the gradient of all variables according to the direction of flow to zero. The no-slip boundary condition is imposed at the oval-sail surface. A symmetry condition is applied on the other boundaries.

2.4 Algorithm and Schemes

The equations are solved by the finite volume method with a fractional time step integration, similar to SIMPLEC algorithm. Variables are collocated at the cell centers. Rhie and Chow interpolation is then used to stabilize pressure oscillations (Archambeau *et al.* 2004). An iterative reconstruction scheme is used to calculate the gradients at the interfaces so that the consistence of the diffusive and the convective fluxes are improved and the order of the numerical scheme for the regions where meshes are non-orthogonal increases (Chaabane *et al.* 2014). To avoid numerical diffusion, a second order UPWIND scheme is applied for the spatial discretization of momentum equations. The convection terms of the turbulent transport equations are discretizd with a first order upwind scheme (it was reported by Hirsch and Tartinville (2009) that the comparison of second order discretisations with first order did not show any significant difference in the results). A first order implicit time integration scheme is used.

All computations are performed with a time step $\Delta t = 10^{-3}$ s. Initial conditions are set to the free stream velocity and turbulence values.

2.5 Relevant Parameters

Fluid forces are calculated by integrating along the sail surface the pressure and viscosity effects. The lift and drag coefficients are then defined as:

$$C_L = \frac{F_y}{0.5\rho U_\infty^2 Lc} \quad (23)$$

$$C_D = \frac{F_x}{0.5\rho U_\infty^2 Lc} \quad (24)$$

where L is the sail span and F_y and F_x are the fluid forces exerted on the body, respectively, in the normal and stream-wise directions. Time-averaged coefficients are computed for a period beginning when periodic vortex shedding occurred.

The vortex shedding frequency f obtained from FFT analysis of the lift coefficient time signal is described by the corresponding non-

dimensional Strouhal number:

$$St = \frac{f\,c}{U_\infty} \tag{25}$$

The pressure distribution at the oval-sail surface is describe by the pressure coefficient:

$$C_P = \frac{p - p_\infty}{1/2\,\rho U_\infty^2} \tag{26}$$

where p is the pressure at the sail surface and p_∞ is the freestream pressure.

In all results discussed here, the magnitude of velocity is normalized by U_∞, the vorticity is presented as dimensionless $\omega^* = \omega c/U_\infty$, the time t is in the non-dimensional form $t^* = U_\infty t/c$ and iso-contours are depicted on a plane located at mid-span of the sail ($z = L/2$).

3. MODEL VALIDATION

Computational grid and turbulence model validations are performed for a circular cylinder, the turbulence being represented by the R_{ij} EBRSM model. These simulations are carried out for an isolated cylinder and for a cylinder with suction control. The Reynolds number based on the free stream velocity and the cylinder diameter (D) is $Re = 10^5$. The obtained results are compared to experimental data reported by Fournier *et al.* (2005).

Computational grid The cylinder is set at the center of an H-domain which extends on a distance equivalent to $5D$ upstream and $30D$ downstream. South and North domain boundaries are located within $\pm 12.5D$. The cylinder span is $4D$. To check the convergence of the solution and ensure grid-independency of the results, three grid resolutions are considered. The relevant details of every mesh are summarized in the Table 4 where N_{cyl} and N_z indicate the number of cells at the cylinder surface and span respectively and N is the total number of cells. The meshes are not uniform, small cells were built near the cylinder wall so that the dimensionless height is $y^+ \approx 1$.

Table 4 Characteristic of the cylinder grids

	N_{cyl}	N_z	N
*Mesh*1	256×15	15	1052190
*Mesh*2	512×15	15	1720110
*Mesh*3	512×30	30	3440220

Model validation is performed for the cylinder without control and with suction control. Suction is applied on a small surface of a width $l_s = 1.4^\circ$ located at $\theta_{cyl} = 90^\circ$ on the upper surface of the cylinder. As in Fournier *et al.* (2005), a momentum coefficient is defined as $C_{\mu cyl} = (2l_s/D)\,(U_{asp}/U_\infty)^2$ where U_{asp} is the suction velocity. Computations with suction control are carried out for $C_{\mu cyl} = 0.3\%$ and $C_{\mu cyl} = 1.0\%$. Experimental values of the drag coefficients are 1.24 for the cylinder without control. For the cylinder with suction control, $C_D = 1.03$ and 1.00 when $C_{\mu cyl} = 0.3\%$ and 1%, respectively.

Non dimensional vortex shedding frequency is calculated from FFT analysis of the time accurate lift curves. For the cylinder without suction, one dominant frequency is found and the related Strouhal number is $St = 0.22$.

The computed mean drag coefficients for the cylinder without suction are 1.30, 1.17 and 1.18 when computations are performed with Mesh 1, Mesh 2 and Mesh 3 respectively. As for the cylinder with suction, the obtained results with the 3 computational grids are respectively, 1.13, 1.13 and 1.06 for $C_{\mu cyl} = 0.3\%$ and 1.18, 1.05 and 0.96 for $C_{\mu,cyl} = 1\%$.

These values are in good agreement with experimental data when computations are performed with the *Mesh*3. However when comparing the results obtained with *Mesh*2 and *Mesh*3, one can notice that increasing the number of cells on the span does not improve significantly the computed values for the cylinder without control.

Since the flow around the cylinder is well predicted, this numerical model is considered able to simulate the flow around the oval-sail. In the following, two computational grids are used: the first one, similar to *Mesh*2 is used for the computation of the flow around the oval-sail without suction. Grids of type *Mesh*3 are applied for the oval-sail with suction.

4. THE OVAL-SAIL WITHOUT SUCTION

These calculations are performed ignoring the fluid area inside the body, without suction and grille. The governing equations are solved for a Reynolds number based on the free stream velocity and the profile chord $Re = 5\,10^5$. All results are discussed for the oval-sail set at a fixed angle of attack $\alpha = 0^\circ$.

4.1 Computational Grid

As previously for the circular cylinder, the oval-sail is set at the center of an H-domain which extends on a distance equivalent to $5c$ upstream

and $30\,c$ downstream. South and North domain boundaries are located within about $\pm 12.5\,c$. The oval-sail span is $4\,c$. Two computational grids of about $3\,10^6$ cells are built, the first one is applied to computations with R_{ij} SSG, the high-Reynolds-number turbulence model and the second grid is applied to computations with both low-Reynolds-number turbulence models ($v2f$ and R_{ij} EBRSM models). Both grids are hybrid type i.e. composed of hexahedral and tetrahedral cells) and generated by block. To ensure accuracy of the solution, highly distorted meshes are avoided. The meshes are not uniform, small cells were built near the oval-sail walls with smooth changes in contigous cell size and shape. In the boundary layer region the cells are hexahedral. It should be noticed that both grids are similar but the height of the first cell raw around the oval-sail walls is reduced for the low-Reynolds-number turbulence grid. Thereby the dimensionless height $y^+ \approx 1$ for $v2f$ and R_{ij} EBRSM computational grid and $y^+ \approx 20$ to 180 for R_{ij} SSG computational grid.

4.2 Lift and Drag Force

The time evolution of the lift and drag forces are depicted in the Fig. 2. as function of the dimensionless time $t^* = U_\infty t/c$. For the sake of clarity, only a period equivalent to $\Delta t^* = 200$ is shown. All curves indicate the unsteady character of the flow. The results obtained with $v2f$ model show that lift curve oscillates periodically with a signal apparent to a sinusoid and that the drag force oscillates at a frequency that is approximately twice the lift force frequency. The Strouhal number highlighted by FFT analysis of the $v2f$ lift curve is about 0.322. The lift curves obtained with both R_{ij} models show more than one oscillation period. However, FFT analysis bring out one dominant frequency corresponding to the Strouhal numbers 0.345 for the R_{ij} EBRSM model and 0.375 for the R_{ij} SSG model (Fig. 3). Loess smooth filter applied to the lift and drag curves indicate that the secondary oscillations of both R_{ij} models have similar periods $\tau_1 \approx 62$ and $\tau_2 \approx 40$ (see Fig. 2).

Mean values of lift and drag coefficients are summarized in the Table 5. It is found that lift coefficient obtained using both $v2f$ and R_{ij} EBRSM models are in good agreement with 3D experimental data of Malavard whereas the C_L value computed by the R_{ij} SSG model is rather close to Malavard's 2D data. These results could suggest that 3D effects are not well modeled by the R_{ij} SSG model. However it is obvious that the difference between C_L values computed with high- and low-Reynolds-

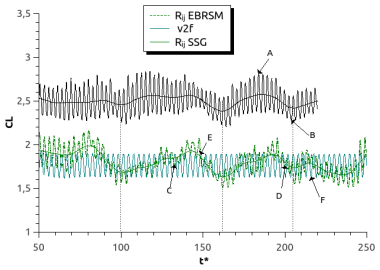

(a) C_L

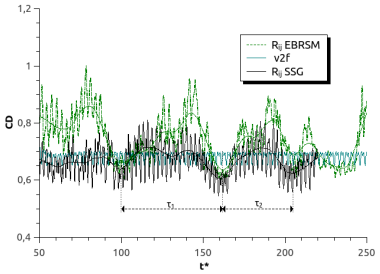

(b) C_D

Fig. 2. Temporal variations of drag and lift coefficients for the oval-sail without suction.

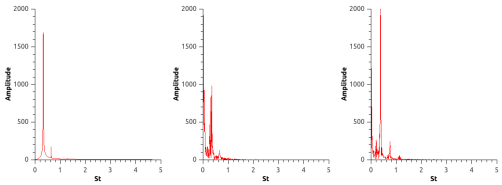

(a) $v2f$ (b) R_{ij} EBRSM (c) R_{ij} SSG

Fig. 3. FFT analysis of the lift curves.

number turbulence models reflects the sensitivity of turbulence modeling to wall pressure prediction. The boundary layer is well resolved by both low-Reynolds-number turbulence models whereas when using high-Reynolds-number turbulence model, boundary layer flow is not accurately predicted in particular when evaluating pressure forces. As regards to the drag coefficient, values computed by all turbulence models are close to Malavard's 2D data (3D data are not available). Then for areas away from the wall as the wake, the flow is well resolved thereby the drag force is better predicted. As bluff bodies aerodynamic drag is dominated by pressure drag, for a better understanding of the flow physics around the oval-sail, the influence of the spoiler on the oval-sail characteristics is analysed in the next section.

4.3 Influence of the Spoiler on the Oval-sail Characteristics

To analyse the influence of the spoiler on the wake, the flow around an oval-sail without

spoiler, called hereafter ellipsoid, is investigated. These computations are carried out using the R_{ij} EBRSM turbulence model. The Reynolds number based on the free stream velocity and the ellipsoid chord is $Re = 5\,10^5$ and the computational grid is similar to that used for the previous computations with both low-Reynolds-number turbulence models.

Streamwise velocity profiles u/U_∞ as a function of y/c are depicted in the Fig. 4. at two streamwise locations in the very near wake, $x/c = 1$ and 2 (Fig. 4(a) and Fig. 4(b)) and further downstream the body at streamwise locations $x/c = 5$ and 6.67 (Fig. 4(c) and Fig. 4(d)). The Fig. 4(e) shows the variation of u/U_∞ as a function of x/c on the wake centerline $y/c = 0.0$. It is seen that in the rear aft body (Fig. 4(a)), the velocity profile of the sail without spoiler exhibits a V pattern whereas the near wake velocity profile of the sail with spoiler is altered from a V shape to zigzag pattern denoting reverse flow on the lower surface. Moreover, it appears that the effect of spoiler increases with an increase in the spanwise distance. At $x/c = 2$, the velocity profiles of the oval sail with spoiler are close to the ellipsoid profiles and symmetrical to the wake centerline (Fig. 4(b)) while further downstream, a larger deviation of the u velocity with respect to the ellipsoid is observed (Fig. 4(c) and Fig. 4(d)). The velocity profiles are altered by the spoiler and asymetrically distributed on the lower side. Then the streamwise velocity profiles of the oval sail with spoiler characterize an expanding wake whereas for the ellipsoid, the vortices path appears to be less important. The simulation results of the oval sail with spoiler predict a curve shifted slightly downward as compared to the profile of the ellipsoid. The vortices path growth in the wake of the oval-sail with increasing distance until about $x/c = 9$ where the wake flow begin to stabilize (Fig. 4(e)).

Figure 4 shows that the flow around the oval sail with spoiler is characterized by a larger region of separated flow. As the free shear layer development determines the pressure rise, then as a direct consequence, large value of the drag coefficient is found. Indeed, the computed mean drag coefficient of the ellipsoid is about 0.376 and unlike the oval-sail with spoiler, the mean lift coefficient is zero. This is due to the symetric geometry of the ellipsoid. When comparing with the drag force of an oval-sail with spoiler, it is found that the spoiler causes an increase of the drag coefficient. The larger drag coefficient of the oval-sail with spoiler is also due to stronger vorticity structure formed in the body

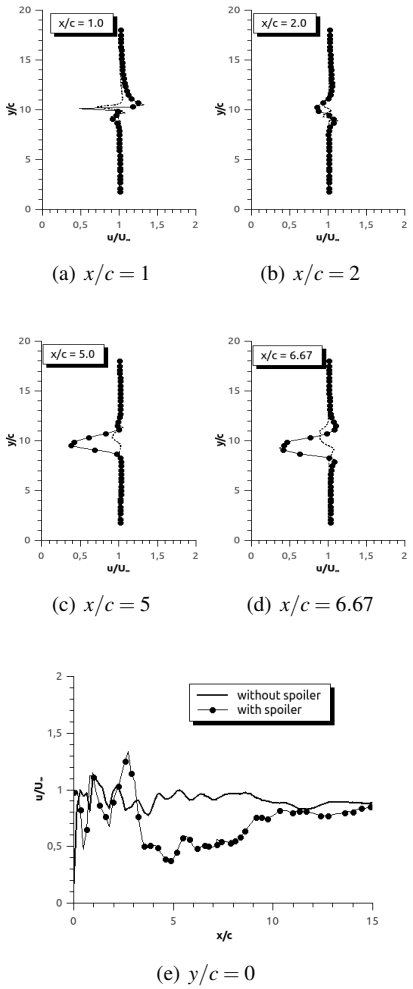

(a) $x/c = 1$ (b) $x/c = 2$

(c) $x/c = 5$ (d) $x/c = 6.67$

(e) $y/c = 0$

Fig. 4. Profiles of the streamwise velocity in the wake of the oval-sail.

wake. So the effect of the spoiler on the flow structure could be assimilated to that of a splitter plate fixed to a circular cylinder. Indeed, it was reported by Bao and Tao (2013), that the secondary vortex formed at the trailing edge of the splitter plate is in the same direction with the main vortex shed from the cylinder, they interact to form a new, stronger vorticity structure, which would increases drag force. This is also observed for the oval-sail with spoiler.

These results show the influence of the spoiler on the flowfield and lift and drag force of the oval-sail. Further numerical investigations on the effect of the spoiler position are ongoing.

Table 5 Forces coefficients of the sail without suction

	SSG	$v2f$	EBRSM	Exp.	
				2D	3D
C_L	2.509	1.771	1.768	2.1	1.9
C_D	0.669	0.683	0.724	0.7	-

4.4 Flow Patterns

Iso-contours of velocity The velocity contours depicted in Fig. 5(a) to Fig. 5(f) at selected times show that similar flow patterns are found with all turbulence models. Flow separation is visible on the upper face of the sail, a recirculation zone is seen around the spoiler and vortices are shed in the wake. The mechanism of vortex shedding is similar to that of a circular cylinder: flow separation on the upper side of the oval-sail feeds a clockwise vortex structure shed in the wake whereas counter-clockwise vortex structure are shed on the lower side.

In Fig. 2(a), points A, B, C, D, E and F show selected times t^* corresponding to the contours depicted in Fig. 5:

- Time represented by point A corresponds to maximal value of the lift coefficient on the R_{ij} SSG lift curve. At that time, a clockwise vortex is shed from the upper surface (Fig. 5 (a)). The time B corresponds to minimal value of the R_{ij} SSG lift coefficient where counter-clockwise vortex is shed from the lower surface (Fig. 5(b)). One can notice that the point B is located on the downward part of the secondary oscillation SSG lift curve.

- Figures 5(b), 5(c) and 5(d) represent the flow patterns at times corresponding to minimal values of the lift coefficient on both R_{ij} lift curves. In spite of this, the three velocity contours are not similar. This difference is attributed to the location of the points B, C and D on the loess smoothing lift curves (Fig. 2). The point C is located on the upward part of the loess smoothing lift curve whereas point D is located on the downward part of this secondary oscillation curve. Figure 5(c) corresponding to time represented by point C shows that the vortex shed by the spoiler are stronger to the flow separation of the upper surface so that the interaction with the upper shear layer creates small spinning vortices.

- Times represented by points E and F correspond to the flow patterns at two opposite positions on the $v2f$ lift curve where clockwise vortex is shed from the upper surface (time E, Fig. 5 (e)) and interact with a counter clokwise vortex shed from the lower surface (time F, Fig. 5 (f)).

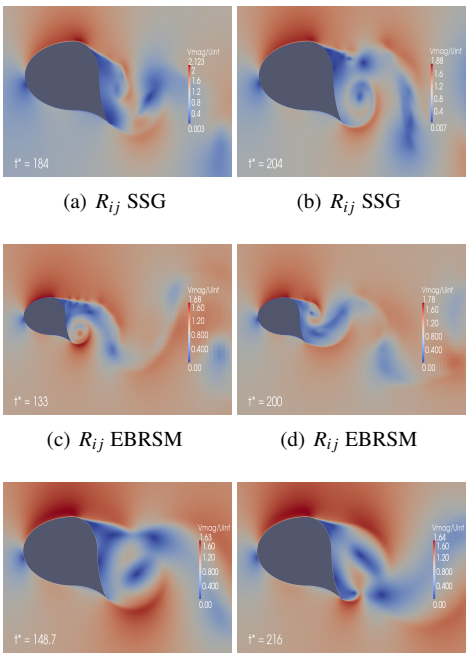

(a) R_{ij} SSG (b) R_{ij} SSG

(c) R_{ij} EBRSM (d) R_{ij} EBRSM

(e) $v2f$ (f) $v2f$

Fig. 5. Contours of velocity magnitude in the vicinity of the oval-sail at two selected times.

Vorticity The contours of vorticity are depicted in Fig. 6. at selected times corresponding to points B, D and F. These figures exhibit one pair of rotating vortices with non-symmetrical pattern. Oscillations of the detached boundary layer at the upper surface of the body (not shown here) have been observed. The contours of vorticity magnitude obtained with both R_{ij} turbulence models (Fig. 6(a) and Fig. 6(c)) indicate that in the mechanism of vortex shedding, both lower and upper vortices interact to create von Karman streets. The vortex paths are larger in the downward part and have two oscillation periods. For a short time, the vortices path is larger than the body thickness.

As for the vorticity contours of $v2f$ turbulence model (Fig. 6(e)), it seems that the vortices are shed alternatively from upper and lower surfaces without a strong interaction. One oscillation frequency corresponding to the vortex detachment is observed. The vortices growth with path amplitude larger than the body thickness in the downstream wake. Both Fig. 6(e) and Fig. 6(f) show that close to the oval-sail, the wake structure appears to be asymmetric, the asymmetry of the flow patterns being driven by the spoiler. Similar wake horseshoes-shape and recirculation lengths are found by both R_{ij} models while the wake recirculation lenght for the $v2f$ seems smaller.

Figures 6(b), 6(d) and 6(f) show the alternates

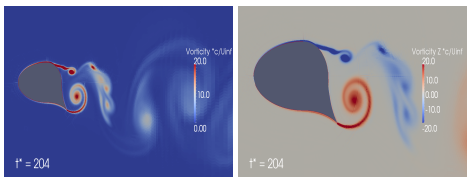

(a) R_{ij} SSG (b) R_{ij} SSG

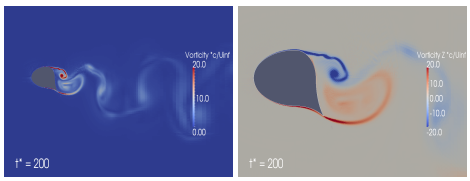

(c) R_{ij} EBRSM (d) R_{ij} EBRSM

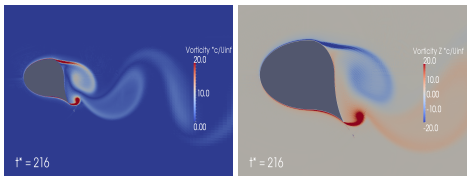

(e) $v2f$ (f) $v2f$

Fig. 6. From left to right, contours of vorticity magnitude and vorticity z in the vicinity of the oval-sail at selected times.

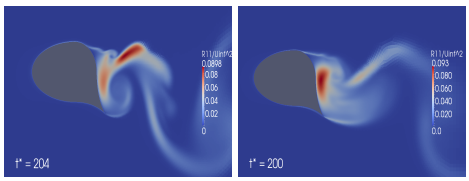

(a) R_{ij} SSG (b) R_{ij} EBRSM

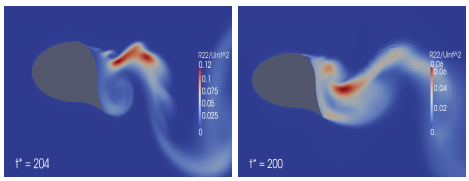

(c) R_{ij} SSG (d) R_{ij} EBRSM

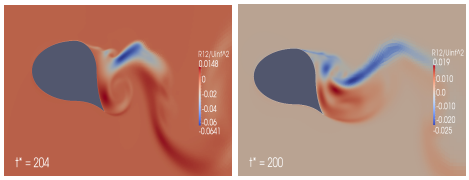

(e) R_{ij} SSG (f) R_{ij} EBRSM

Fig. 7. From top to down, contours of r_{11}/U_∞^2, r_{22}/U_∞^2 and r_{12}/U_∞^2 in the vicinity of the oval-sail at selected times corresponding to points B and D for R_{ij} SSG and R_{ij} EBRSM.

eddies with positive and negative z-directed (span-wise) vorticity.

Figures 5 and 6 show that two vortices of unequal size and opposite sign are shed alternatively from both sides of the sail with spoiler. The shedding vortices mechanism produces as follow: The flow is accelerated along the sail upper surface and then separation occurs. On the lower surface, the spoiler deviates the flow and creates a clearly visible reversed flow zone which provides the fluid mass for the lower vortex creation. These figures show that similar flow patterns are predicted by all turbulence models. However, vortex shedding frequencies are different.

Turbulence quantities The contours of Reynolds stress tensor components obtained by both R_{ij} models are similar (see Fig. 7). However, the transverse Reynolds stress values of the R_{ij} SSG are slightly larger than the R_{ij} EBRSM model. By contrast, the streamwise Reynolds stress and Reynolds shear stress are lower.

As for the ratio μ_t/μ, values computed by R_{ij} SSG are slightly larger than that of R_{ij} EBRSM. Even larger values are calculted by $v2f$ model (Fig. 8).

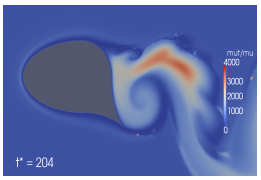

(a) R_{ij} SSG

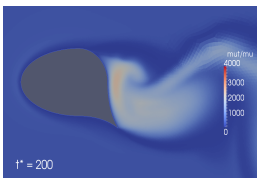

(b) R_{ij} EBRSM

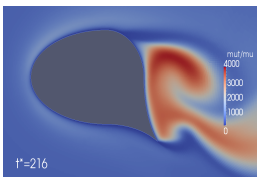

(c) $v2f$

Fig. 8. Contours of μ_t/μ in the vicinity of the oval-sail at times corresponding to points B, D and F for R_{ij} SSG, R_{ij} EBRSM and $v2f$ model respectively.

4.5 Comments

Several uncertainties can affect numerical simulations based on linear eddy-viscosity hypothesis as the presence of high curvature or stagnation point anomaly: (i) According to Leschziner (2001), model based on linear eddy-viscosity hypothesis perform well in relatively simple strain but often do badly in the presence of high curvature. (ii) It was reported that two-equations models predict an anomalous large growth of turbulent kinetic energy in stagnations flows and even when the stagnation region is not of interest per se, this spurious behavior can upset the rest of flow computations (Durbin 1996). Then, the $v2f$ model is not fully satisfactory because it still uses the eddy viscosity hypothesis (Manceau and Hanjalic 2002).

Furthermore, in a comparative study performed by Billard *et al.* (2012), the superiority of R_{ij} EBRSM model was revealed for solving flows with 3D effects and recirculation areas. It appears that so is in these simulations. Indeed, it is noticed that flow patterns found by both R_{ij} models are similar but mean values of lift coefficients are different. Due to good resolution of the boundary layer by both low-Reynolds-number turbulence models, lift coefficients calculated by R_{ij} EBRSM and $v2f$ models are close to experimental data. The R_{ij} SSG model gives a correct prediction sufficiently far from the wall, but does not reproduce the damping of the redistribution very close to it. In other words, with this high-Reynolds-number turbulence model, boundary layer flow is not accurately predicted in particular when evaluating pressure while the wake flow is well resolved by both R_{ij} models.

As both boundary layer and wake areas are well computed by R_{ij} EBRSM turbulence model, it is applied for the following simulations of the fluid flow around the oval-sail with suction.

5. THE SAIL WITH SUCTION

As mentioned previously, the oval-sail has to be used as a wind assisted propulsion device. Therefore, suction flow control is applied for decreasing drag and increasing lift. The oval-sail is equipped with a suction-grid located on the upper side, all along the span, in areas where the flow separates. Air suction is carried out at the lower face of the body. The suction-grid is defined by an angle width, θ and a number of slots, n or the slot width, ls (Fig. 1). In practical approach, the suction is imposed using a fan at the lower face of the oval sail. In these numerical simulations, suction is modeled imposing a uniform flow rate Q at the circular bottom face of the oval sail. The flow rate Q is calculated according to the following suction coefficient :

$$C_Q = \frac{Q}{U_\infty c L} \tag{27}$$

where L is the sail span. In the following computations, the suction coefficient has a fixed value ($C_Q = 0.47$). The changing parameters are the angle θ and the number of slots n whose values are summarized in the Table 5. It should be noticed that other control parameters could affect the aerodynamic performance of the sail such as position of the spoiler, aspiration rate (or C_Q) and orientation of the sail to the incident wind. The parameters selected here are a preliminary study. Further work is ongoing where the influence of aspiration rate and angle of incidence of the oval-sail are investigated. In the present work, the aerodynamic lift and drag forces, the topology of the mean flow in the wake and the vortex shedding frequency are thus analyzed as function of the suction-grid geometry, for a fixed value of the momentum coefficient. The governing equations are solved for a Reynolds number based on the free stream velocity and the profile chord $Re = 5\,10^5$.

5.1 Computational Grid

The computational domain used for the oval-sail with suction is depicted in Fig. 9(a). The meshes are modified to include the slots (see Fig. 9(b)) then a specific grid of more than $7\,10^6$ cells is built for each case. The height of the first cell row y_0 is defined so that the dimensionless height $y^+ \approx 1$.

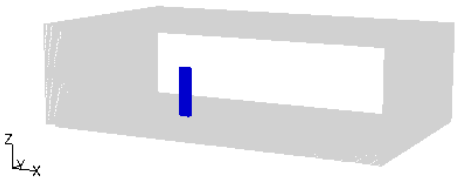

(a)

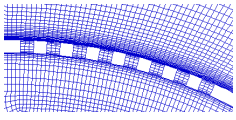

(b)

Fig. 9. Computational domain and mesh around the slots in the case of the sail with suction.

As previously for the oval-sail without suction, velocity magnitude and vorticity are given in dimensionless form (normalized by U_∞ and c/U_∞,

respectively) and all contours are depicted on the plane $z = L/2$ located at mid-span of the sail.

Table 6 Suction grille parameters

case	24-8	36-8	48-5	48-8
θ	24°	36°	48°	48°
n	8	8	5	8
l_s	1.5°	2.25°	4.8°	3°

5.2 Flow Patterns

Vorticity iso-contours around the oval-sail with suction are represented in Fig. 10. and 11. It is seen that the suction modifies the wake flow topology. The massive turbulent separation on the upper side of the body does not occur. Separation is laminar and delayed near the trailing edge, on the spoiler. It appears that vortex shedding on the upper side of the sail are attenuated (case 24-8) or suppressed by suction whereas the vortex shedding on the other side is not influenced. In both figures, it is seen that the vortex shedding suppression effect is improved when the grid expansion increases. Then as it is verified in next section, the point of separation is delayed to the trailing edge when θ increases.

Both figures show the remaining vortices generated by the spoiler and internal vortices attached to the cylindrical wall. In analogy to the work presented by Kourta (2004), the internal vortices are associated to parietal vortices related to a pure hydrodynamical instability. Indeed, from the internal cylindrical part of the sail, suction can be seen as flow injection through the slots. These internal vortices are interpreted as the Gortler vortices that may occur in concave-wall boundary layers due to centrifugal instability (Wadey 1992).The Gortler instability is characterized by a Gortler number $Go = \sqrt{ReL_{ref}/R}$ where L_{ref} is a reference lenght and R is the wall curvature. In our case, $L_{ref} = c$ and the resulting Gortler number is large ($Go = 1227$). According to (Wadey 1992), at large Gortler number, the mean flow is an order of magnitude smaller to the disturbances it creates and the effect of increasing the Gortler number is to force the layer of activity away from the wall. These phenomenon are observed in the contours of internal vortices and seem influenced by the larger of slots l_s.

As for the near wake, one pair of vortices are shed but they are no longer apparent. The wake vortices are two vortex filaments downward directed. The remaining vortices are due to flow deviation caused by the spoiler and are related to Kelvin-Helmotz instabilities (Kourta 2004).

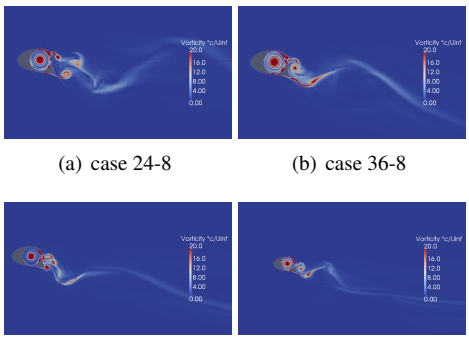

(a) case 24-8 (b) case 36-8

(c) case 48-5 (d) case 48-8

Fig. 10. Iso-contours of the vorticity magnitude in the wake of the oval-sail with suction.

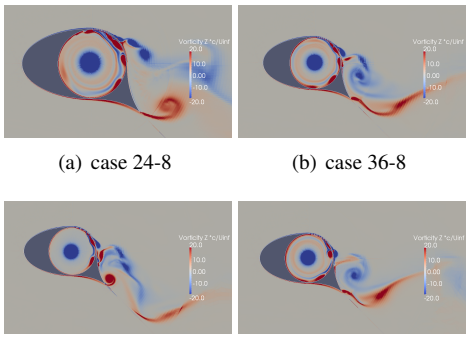

(a) case 24-8 (b) case 36-8

(c) case 48-5 (d) case 48-8

Fig. 11. Iso-contours of the vorticity Z in the wake of the oval-sail with suction.

5.3 Pressure

In Fig. 12. are depicted time-averaged pressure coefficient distributions at the surface of the oval sail with suction (Fig. 12(a) and 12(b)) and for comparison at the surface of the oval sail without suction (Fig. 12(c)). Pressure coefficients are plotted as a function of x/c, where x is the horizontal coordinate of the sail. The location of the separation on the upper surface of the oval sail are indicated in the Fig. 12(d). Pressure surface distribution indicates that separation on the upper surface occurs at about $\theta_0 = 120°$ for the oval without suction. As for the oval sail with suction, separation on the upper surface occurs at about $\theta_1 = 135°$ for the case 24-8 while for the 3 others cases, separation is located at about $\theta_2 = 157°$.

5.4 Lift and drag forces

To quantify the drag reduction and lift improvement, the mean lift and drag coefficients of the controlled sail are normalized by their corresponding values of the baseline case (without suction control). Thus lift and drag coefficients are given in Table 7 by the ratios C_{LS}/C_L and

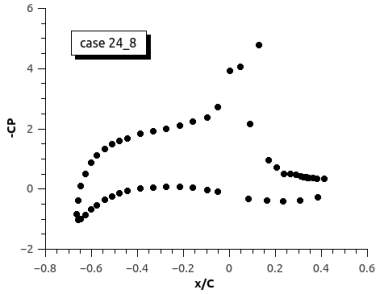

(a) case 24-8

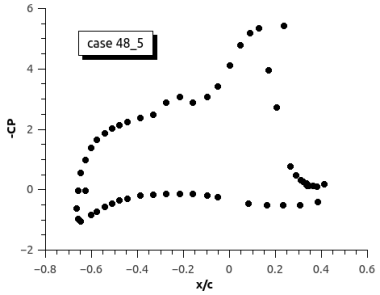

(b) case 48-5

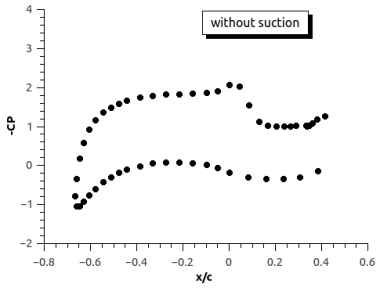

(c) without suction

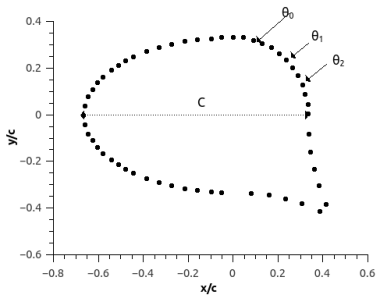

(d)

Fig. 12. Pressure surface distribution on the oval sail with suction ((a) and (b)), without suction (c) and location of the flow separation (d).

C_{DS}/C_D where C_{LS} and C_{DS} are lift and drag coefficients of the sail with suction. In propulsive devices, the lift to drag ratio is an important parameter in the design process as it determines the maximum power that can be reached.

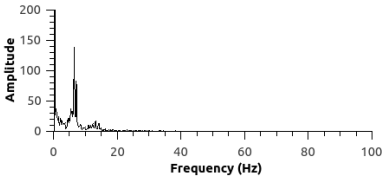

(a) case 36-8

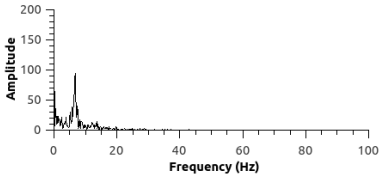

(b) case 48-5

Fig. 13. FFT of the lift coefficient for the oval sail with suction.

Table 7 Lift and drag coefficients of the sail with suction

case	24-8	36-8	48-5	48-8
C_{LS}/C_L	1.01	1.20	1.44	1.40
C_{DS}/C_D	0.42	0.41	0.37	0.36
C_{LS}/C_{DS}	5.85	7.07	9.44	9.54
St	0.051	0.052	0.057	0.056
τ^*	19.6	19.0	17.6	17.8

Therefore C_{LS}/C_{DS} ratio values are also given in the Table 7.

For all cases, it is found a high decrease of the drag coefficient. As for the lift coefficient, $C_{LS}/C_L = 1.01$ for case 24-8, thus the lift force is not improved when the grid width is $\theta = 24°$. When $\theta \geq 36°$, the lift improvement reaches more than 20%. Higher lift coefficient is get for the widthest suction grille. As for the slots number, a slight decrease of the lift and drag coefficients is observed when the number of slots increases (i.e. when the slot width decreases). As a consequence, the 8 slots grid have slightly lower C_{LS}/C_{DS} ratio however this improvement is not important. Thus one can just notice that better overall performances are obtained with the widest grid.

Furthermore, the mean lift coefficient computed for the case 48-8 is closed to experimental data of Malavard (1984). The latter found that the lift coefficient of 66% thick section profile with suction coefficient $C_Q = 0.05$ was $C_{LS} = 2.6$, leading to the ratio $C_{LS}/C_L = 1.37$.

FFT analysis applied to the lift curves bring out one dominant frequency for each case (see Fig. 13). It is seen that the value of the main peak in the spectrum of lift is reduced compared to

the oval-sail without suction of the Fig. 3. The related non dimensional Strouhal number vary from $St = 0.051$ for the case 24-8 to $St = 0.057$ for the case 48-5 (see Table 7). Thus the vortices shedding frequency is highly reduced and it appears that the Strouhal number increases as the lift coefficient. So it is noticed that the related dimensionless period τ^* is about one half the secondary oscillation period that was observed for the oval sail without suction. Therefore as it was observed by Ye Jun Chen and Chuan Ping Shao (2013), the unilateral shedding frequency is nearly equal to the frequency of alternative vortex shedding of the oval sail without suction.

6. CONCLUSION

Turbulent fluid flow computations have been performed for an investigation of suction effect on the aerodynamic performance of an oval-sail. Three turbulence models were first applied for the sail without suction: the $v2f$, an eddy viscosity model and two Reynolds stress models (R_{ij} SSG and R_{ij} EBRSM models). Similar flow patterns were obtained with all URANS models. Contours of velocity and vorticity around the bluff body without suction exhibit highly complex flow with Von Karman street vortices in the wake. Expected mean lift and drag coefficients have been obtained with both low-Reynolds-number turbulence model. As the R_{ij} EBRSM was the most efficient turbulence model for solving the flow field, it was applied for the simulation of the flow around the oval-sail with suction.

Then, the influence of the suction on the flow field and profile performances is considered. Due to centrifugal instability, Gortler vortices are observed on the internal curved surface of the sail. On the external upper surface of the sail, separation is delayed. As expected, it is found that the aerodynamic performances of the sail are improved. Better lift to drag ratio is obtained when the grid width and the slots number increase. Moreover, vortex shedding is suppressed by the suction. It is thus expected that vortex induced vibrations will not occur.

ACKNOWLEDGMENTS

The authors kindly acknowledge financial support from FEDER for this work.

REFERENCES

Amitay, M. and Glezer A. (2002). Controlled transients of flow reattachment over stalled airfoils. *International Journal of Heat and Fluid Flow 23*, 690-699.

Archambeau, F., Mechitoua N. and Sakiz, M. (2004). Code_saturne: a finite volume code for the computation of turbulent incompressible flows: industrial appication. *Internationa Journal on Finite Volumes 1*, 1–62.

Bai, Y. L., Ma X. Y. and Ming X. (2011). Lift enhancement of airfoil and tip flow control for wind turbine. *Applied Mathematics and Mechanics (Engl. Ed.) 32*, 825–836.

Bao, Y. and Tao J. (2013). The passive control of wake flow behind a circular cylinder by parallel dual plates. *Journal of Fluids and Structures 37*, 201–219.

Basara, B. and Bachier, G. and Schiffermuller, H. (1997). Calculation of vortex shedding from bluff bodies with the Reynolds Stress Model. *Fifteenth International Conference on Numerical Methods in Fluid Dynamics. Lecture Notes in Physics 490*, 534–539.

Billard, F., Revell, A. and Craft T. (2012). Application of recently developed elliptic blending based models to separated flows. *International Journal of Heat and Fluid Flow 35*, 141–151.

Boccaletti, G., R. Ferrari and B. Fox-Kemper (2005). Controle par rotation ou par aspiration de l'écoulement autour d'un cylindre calculé par Simulation des Grandes Echelles. *Comptes rendus de mécanique 333*, 273–278.

Boccaletti, G., R. Ferrari, and B. Fox-Kemper (2004). Numerical study of blowing and suction control mechanism on NACA0012 airfoil. *Journal of Aircraft 41*, 1005–1013.

Chaabane Khelifi, S., Mechitoua N., Hulsemann F. and Magoules F. (2014). A hybrid multigrid method for convection-diffusion problems. *Journal of Computational and Applied Mathematics 259 Part B*, 711–719.

Chen, Y. J. and C. P. Shao (2013). Suppression of vortex shedding from a rectangular cylinder at low Reynolds numbers. *Journal of Fluids and Structures 43*, 15–27.

Durbin P. A. (1996). On the k-3 stagnation point anomaly. *Int. J. Heat and Fluid Flow 17*, 89–90.

Favier, J. and Kourta A. (2006). Etude du controle du décollement sur un profil d'aile par mesures PIV et analyse POD.

Comptes rendus de mécanique 334, 272–278.

Godard, G. and Stanislas, M. (2006). Control of a decelerating boundary layer. Part 1: Optimization of passive vortex generators. *Aerospace Science and Technology 10*, 181–191.

Hirsch, C. and Tartinville B. (2009). Reynolds-Averaged Navier-Stokes modelling for industrial applications and some challenging issues. *International Journal of Computational Fluid Dynamics 23*, 295–303.

Kourta, A. (2004). Instability of channel flow with fluid injection and parietal vortex shedding. *Computers and fluids 33*, 155–178.

Laurence, D. R., Uribe J. C. and Utyuzhnikov, S. V. (2004). A robust formulation of the $v2-f$ model. *Flow, Turbulence and Combustion 73*(3), 169–185.

Leschziner M. A. (2001). Mixed Layer Instabilities and Restratification. *Journal of Physical Oceanography 37*(9), 2228–2250.

Leschziner M. A. (2001). Statistical turbulence modelling for the computation of physically complex flows. *In Course 4.* EDP Sciences Springer-Verlag.

Lim, H. C. and Lee S. J. (2004). Flow control of a circular cylinder with O-rings. *Fluid Dyn. Res.n 35*, 107–122.

Malavard, L. (1984). Un nouveau propulseur éolien de navire. *La vie des Sciences 1*, 57–72.

Manceau, R. and Hanjalic, K. (2002). Elliptic blending model: a new near-wall Reynolds stress turbulence closure. *Physics of Fluids 14*, 744–754.

Muddada, S. and Patnaik, B. S. V. (2010). An active flow control strategy for the suppression of vortex structures behind a circular cylinder. *European Journal of Mechanics B/Fluids 29*, 93–104.

Reddy, M., Muddada S. and Patnaik B. S. V. (2013). Flow past a circular cylinder with momentum injection: optimal control cylinder design. *Fluid Dyn. Res. 45*, 015501.

Roumeas, M., Gillieron P. and Kourta A. (2009). Analysis and control of the near wake flow over a square back geometry. *Computers and fluids 38*, 60–70.

Seifert J. (2012). A review of the Magnus effect in aeronautics. *Progress in Aerospace Science 55*, 17–45.

Speziale, C. G., S. Sarkar and T. B. Gatski (1991). Modelling the pressure-strain correlation of turbulence: an invariant dynamical systems approach. *J. Fluid Mech. 227*, 245–272.

Viswanath, P. R., Ramesh G. and Madhavan K. T. (2000). Separation control by tangential blowing inside the bubble. *Experiments in Fluids 29*, 96–102.

Wadey, P. D. (1992). On the development of Gortler vortices in wall jet flow. *Journal of Engineering Mathematics 26*, 297–313.